2024 IEEE/RSJ International Conference on Intelligent Robots and Systems (IROS)
October 14-18, 2024. Abu Dhabi, UAE

A Circular Soft Pneumatic Actuator with Bi-Directional Bending Behavior

Jeannette Circe[1], Michael Giglia[1], Isaiah Rivera[1], Ani Vardanyan[1], Brandon Bunt[1], and Michelle H. Rosen[1]

***Abstract*— Most existing soft robotic actuators require multiple chambers to achieve multi-directional bending. In this paper, we present the design, fabrication, and analysis of a novel circular actuator. The actuator is made from a single soft material and is capable of bi-directional bending using only positive pressure in a single chamber. To accurately predict the required pressure for all bending angles, we developed an analytical model for the full range of motion - both uncurling and curling. We tested and analyzed actuators fabricated out of four types of silicone and found that the softest actuators have a bending range from the initial bending angle, 210°, to 0°, and to 225° in the other direction in 112 kPa. When constraining the actuators, we found they can create up to 5.1 N of blocked force in 210 kPa. Additionally, we demonstrate that a single circular actuator can grasp objects of various weights up to 800 g from both the inside and outside.**

I. INTRODUCTION

Soft robots are safer for human interaction than traditional robots and are often used in grasping applications due to their inherent compliance and adaptability [1], [2]. With changes in internal pressure, soft pneumatic actuators can generate motions such as bending, twisting, and extending. These behaviors rely on pre-programmed asymmetries in material stiffness or geometry [3]–[5]. Simple bending pneumatic actuators generally consist of an inflatable chamber constrained in one or more directions by inextensible materials, resulting in motion along a single degree of freedom. To achieve multi-directional bending, multiple simple chambers can be connected in parallel [6], [7]. Placing several of these multi-chambered actuators in series allows for an extensive range of motion with multiple degrees of freedom [8]–[10]. Many actuators can grasp objects in multiple orientations by using these additional degrees of freedom [11] or combinations of positive and negative pressure [12].

Increasing the number of independently actuated chambers enables a wider range of motion but requires more complex control. Increasing the bending capabilities with fewer chambers can require two regulators to generate both positive and negative pressure [13]. Advancing the field requires developing soft robots with more types of achievable motion from each control input, simplifying possible applications by reducing the number of control inputs per robot [14].

Initially-straight actuators are generally easy to fabricate but are limited in their useful range of motion. Fabricating actuators with curvature or an initial bending angle allows for more efficient motion and a greater range of bending angles by reducing the material strain [15]. Previous examples of circular pneumatic actuators had a closed circle configuration and could grasp objects but could not bend [16]. Other pre-curved actuators consisting of a single chamber composed of two silicones could only uncurl or curl further based on which side has stiffer silicone [17]. These actuators generate either curling or uncurling motion with a single control input; however, they require complex fabrication techniques, with multiple soft materials and fiber wrapping. No single-chamber soft pneumatic actuator made of a uniform soft material has demonstrated both uncurling and curling bending behavior only with positive pressure input.

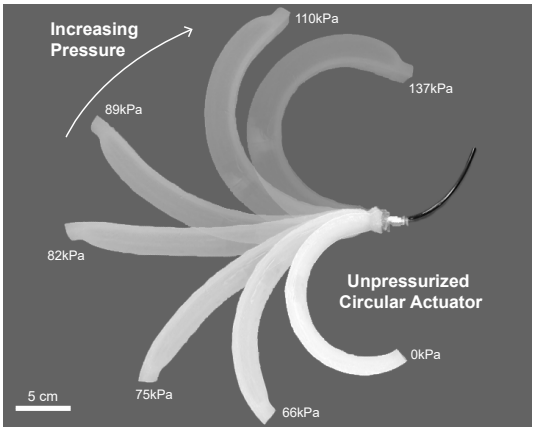

Fig. 1. A circular soft pneumatic actuator made of Dragon Skin 20 silicone at seven different input pressures. With increasing pressure, the actuator first uncurls fully before curling again in the opposite direction.

We present a circular soft pneumatic actuator with bi-directional bending from a single positive pressure source. As shown in Fig. 1, with increasing pressure, the circular soft pneumatic actuator fully uncurls and then curls back on itself. Our actuator achieves this large workspace by pressurizing just one chamber and a single control signal. This allows for grasping both by uncurling inside the object and by curling around the outside of the object, which will allow additional dexterity in object manipulation tasks.

In this paper, we describe the fabrication process and present an analytical model for all bending angles as a function of input pressure, including circumferential and radial deformation. Additionally, we present an experimental procedure for characterizing the bending behavior and blocked force of actuators made from four materials. We also demonstrate force-based grasping from both the inside and outside of objects.

[1]Albert Nerken School of Engineering, The Cooper Union for the Advancement of Science and Art, New York, NY 10003, USA circe@cooper.edu, michael.giglia@cooper.edu, michelle.rosen@cooper.edu

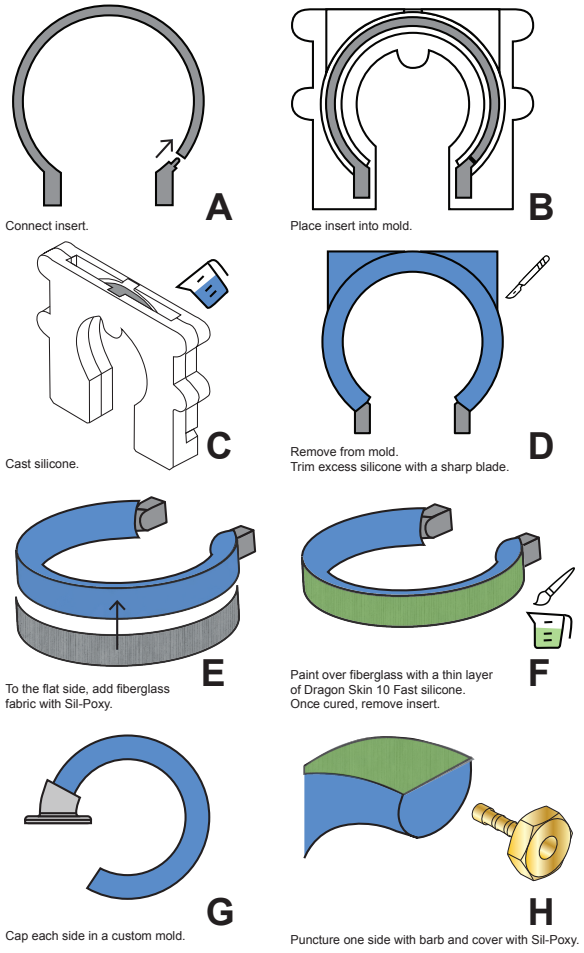

Fig. 2. The simple fabrication process of the circular actuator.

II. METHODS

A. Fabrication

To create the circular actuators we use a single-material casting procedure with 3D-printed molds. We chose a semi-circular cross-section for its small bending resistance [18]. To form the inner chamber, a 3D-printed, two-piece insert, which comes apart for easy removal, snaps into the mold (Fig. 2A). The insert is rigidly constrained in the center of the mold so that the silicone walls have a constant thickness along the actuator and to ensure consistent fabrication between actuators (Fig. 2B). To characterize how the actuator's behavior changes with material, we used four different two-part silicones with Shore A Hardness ranging from 20–50: Dragon Skin 20 (DS20), Dragon Skin 30 (DS30), Smooth Sil 940 (SS40), and Smooth Sil 950 (SS50) (Smooth-On, USA). We mix, degas, and pour the silicone inside the opening at the top of the mold (Fig. 2C). After casting, we leave the actuator to cure at room temperature according to the manufacturer's instructions.

After curing, we remove the actuator from the mold and cut away excess material (Fig. 2D), leaving the insert inside to ensure we add no additional stress. We add a strip of fiberglass fabric (4 oz S-glass, US Composites) to the flat side of the cross-section with Sil-Poxy (Smooth-On, USA) (Fig. 2E). We paint a thin layer of Dragon Skin 10 Fast (SmoothOn, USA) over the fiberglass to ensure a secure attachment to the actuator (Fig. 2F). No other strain-limiting materials are required to achieve the bi-directional bending behavior, significantly simplifying and the fabrication process.

After removing the insert, we seal both ends with the same silicone used for the actuator body using a 3D-printed mold (Fig. 2G). To create a secure connection to the pressure input, we attach custom-machined barbs by puncturing one side of the actuator and coat the interface with Sil-Poxy to ensure an airtight connection (Fig. 2H).

B. Analytical Model for Bending Angle

To characterize the actuator's bending behavior as a function of input pressure and material properties, we develop an analytical model for curling and uncurling based on those found in [17]–[19]. Fig. 3 defines the geometric variables used throughout the model. We calculate the input pressure P required to reach a given bending angle ψ using the geometry of the actuator, the length of the inextensible layer l_0, and the non-linear hyperelastic material properties of each silicone, including non-axial deformation. To account for circumferential deformation, we transform the cross-section at each pressure based on material stretches. As the pressure increases, the actuator uncurls (decreasing ψ from its initial bending angle ψ_0 to an angle $\psi = 0$, where the actuator is straight. Further increasing pressure causes ψ to become negative, corresponding to curling behavior, thus generating a bi-directional range of motion (Fig. 3A).

As the actuator bends, the silicone stretches in the axial direction to maintain the length l_0 of the inextensible layer. The model assumes that the actuator maintains a single, constant bending radius along its length at all pressures and that the cross-section remains orthogonal to the inextensible layer. We also assume incompressibility in the hyperelastic material, such that $\lambda_1\lambda_2\lambda_3 = 1$ where λ_i is the stretch ratio in each direction (axial, circumferential, and radial, respectively). This assumption requires that the cross-sectional area of the silicone remains constant, even as the shape deforms. Increasing pressure causes the semi-circular region to expand outwards into a circular shape, resulting in thinning of the actuator's walls to maintain a constant cross-sectional area (Fig. 3D). We assume no geometric changes in the base layer because of the proximity to the inextensible layer.

For the undeformed cross section, as shown in Fig. 3B, β is the coordinate in the base layer away from the inextensible layer, and τ is the distance from the inner wall in the φ direction. The base region has thickness b = 0.38 cm, and the undeformed semi-circular cross-section wall has radius a_0 = 0.64 cm and thickness t_0 = 0.38 cm. In the deformed cross-section (Fig. 3D), we assume that the silicone forms a circular arc with offset from the base q, inner radius a, wall thickness t and angle range $-\varphi_m$ to φ_m. τ' and φ' are scaled coordinates with reference to the undeformed shape such that $\tau' = \tau\frac{t}{t_0}$ and $\varphi' = \varphi\frac{2\varphi_m}{\pi}$.

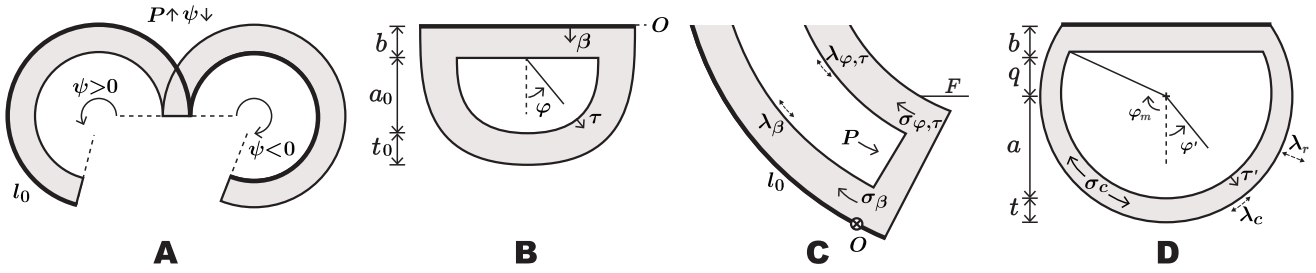

Fig. 3. Geometric variables defined for the analytical model. The thicker line represents the inextensible layer. (A) Definition of positive and negative bending angles. (B) Undeformed cross-sectional geometry of the actuator. (C) Axial stretch ratios and corresponding stress in response to applied pressure. (D) Deformed cross-sectional geometry to account for circumferential and radial deformation.

For a given bending angle ψ, we calculate the axial stretch ratio λ_1 as λ_β for material in the base and $\lambda_{\varphi,\tau}$ in the semi-circular region (Fig. 3C). When ψ is negative, the axial stretch ratio $\lambda_1 \geq 1$ as all lengths must exceed l_0. We also calculate the circumferential stretch ratio $\lambda_2 = \lambda_c$. These equations hold for the entire range of ψ and deformation of the cross-section.

$$\lambda_1 = \lambda_\beta = \frac{l_0 - \beta\psi}{l_0 - \beta\psi_0} \tag{1}$$

$$\lambda_1 = \lambda_{\varphi,\tau} = \frac{l_0 - (b + q + (a + \tau')\cos\varphi')\psi}{l_0 - (b + (a_0 + \tau)\cos\varphi)\psi_0} \tag{2}$$

$$\lambda_2 = \lambda_c = \frac{2(a + \tau')\varphi_m}{(a_0 + \tau)\pi} \tag{3}$$

For the undeformed shape, the circumferential stretch ratio λ_2 is 1. The stretch ratio in the radial direction $\lambda_3 = \lambda_r$ can be calculated as $\lambda_3 = 1/(\lambda_1\lambda_2)$ from the incompressibility assumption. To find the wall thickness t of the circular arc region of the deformed cross-section, we integrate the radial stretch of the undeformed shape over the thickness:

$$t = \int_0^{t_0} \frac{1}{\lambda_{\varphi,\tau} \times 1} d\tau \tag{4}$$

To account for the inaccuracy of the material models and the compressibility of the Dragon Skin materials, we scale the calculated thickness by $k_t(1 - |\psi - \psi_0|/\psi_0)$ where $k_t = 0.3$ is a constant determined by best fit to the experimental expansion results. This scaling accounts for the non-zero radial stress, especially at negative bending angles. No scaling is necessary for the stiffer Smooth Sil materials.

To transform the cross-section from the original semi-circle to the circular arc, we use the scaled thickness t and the cross-sectional area A_0 to calculate the deformed inner radius a, angle range $2\varphi_m$, and vertical offset q:

$$\frac{A_0}{2\sin\varphi_m t} - \frac{t}{2} = \frac{a_0}{\sin\varphi_m} \tag{5}$$

$$a = \frac{A_0}{2t\varphi_m} - \frac{t}{2} \tag{6}$$

$$q = -a\cos\varphi_m \tag{7}$$

TABLE I
MATERIAL PROPERTIES USED IN ANALYTICAL MODEL

	Variable	Value	Unit
DS20 [20]	μ_1, μ_2, μ_3	-0.9534, -1.4515, 2.4085	MPa
	α_1, α_2, α_3	3.478, 3.181, 3.339	
DS30 [20]	μ_1, μ_2, μ_3	0.03816, 0.02524, 0.04456	MPa
	α_p	3.417	
SS40 [21]	μ_1	0.24	MPa
	α_1	2	
SS50 [22]	μ_1	0.68	MPa
	α_1	2	

The axial and circumferential stretch ratios are then recalculated using the deformed cross section and Equations 1–3 before calculating stress with the material model.

To describe the stress-strain relationship for each of the soft materials, multiple material models are available; they can vary significantly in accuracy depending on the amount of strain [23]. We choose the Ogden hyperelastic material model because it is more accurate at higher stretches and for softer materials [20]. The strain energy density function W for the Ogden model is given by:

$$W = \sum_{p=1}^{N} \frac{\mu_p}{\alpha_p}(\lambda_1^{\alpha_p} + \lambda_2^{\alpha_p} + \lambda_3^{\alpha_p} - 3) \tag{8}$$

where μ_p and α_p are experimentally determined material coefficients. We can use a given Neo-Hookean material model coefficient (μ) in the Ogden model by setting $N = 1$ and $\alpha_1 = 2$ in (8). The Cauchy stresses in all three directions are given by $\sigma_j = -p + \lambda_j \frac{\partial W}{\partial \lambda_j}$, where p is a Lagrange multiplier. The stresses in the radial direction are significantly smaller than those in the other directions, so we assume $\sigma_3 = 0$. We calculate the axial and circumferential stresses using:

$$\sigma_1 = -p + \mu_1\lambda_1^{\alpha_1} + \mu_2\lambda_1^{\alpha_2} + \mu_3\lambda_1^{\alpha_3} \tag{9}$$

$$\sigma_2 = -p + \mu_1\lambda_2^{\alpha_1} + \mu_2\lambda_2^{\alpha_2} + \mu_3\lambda_2^{\alpha_3} \tag{10}$$

$$p = \mu_1(\lambda_1\lambda_2)^{-\alpha_1} + \mu_2(\lambda_1\lambda_2)^{-\alpha_2} + \mu_3(\lambda_1\lambda_2)^{-\alpha_3} \tag{11}$$

The bending moments M_P and M_σ about the O axis (Fig. 3C) result from pressure on the end of the actuator and axial stress, respectively. These moments must be equivalent for the actuator to achieve static equilibrium. We calculate the bending moment M_σ as the integral of the force from axial stress in both the base (σ_β) and the circular arc ($\sigma_{\varphi,\tau}$) regions times the orthogonal distance from O for the entire length of the actuator.

$$M_\sigma = 2l_0 \int_0^b \sigma_\beta (a_0 + t_0)\beta d\beta + l_0 \int_0^{t_0} \int_{-\frac{\pi}{2}}^{\frac{\pi}{2}} \sigma_{\varphi,\tau}((a+\tau')\cos\varphi' + b + q)(a+\tau')d\varphi d\tau \quad (12)$$

The bending moment M_P resulting from a given input pressure P acting on the end of the actuator is a function of the deformed cross-sectional geometry:

$$M_P = P \int_{-\frac{\pi}{2}}^{\frac{\pi}{2}} \int_0^a a(b + q + a\cos\varphi) d\varphi da = \frac{4a^3 + 3\pi a^2(b+q)}{6} P \quad (13)$$

We equate (12) and (13) and solve for the required input pressure P to induce the axial stresses for a given bending angle ψ. To account for the underestimation of P due to uncertainty in the material models and non-uniformity in the actuator, we scale the calculated pressure by a constant k_P, determined by a best fit for each material. k_P is 3.8 for DS20, 1.8 for DS30, and 2.2 for SS40 and SS50.

C. Experimental Setup

We characterize the behavior and capabilities of the actuators in response to pressure changes using a custom experimental setup as shown in Fig. 4A. A voltage-adjustable pressure regulator (ITV1031, SMC) controls the input pressure to the actuator. The source pressure comes from a reservoir continuously pressurized to 250 kPa $\pm$ 35 kPa, which acts as a buffer, preventing the need for complex control on the compressor to regulate actuator pressure. We control the experimental setup components with a Raspberry Pi Pico microcontroller which communicates over SPI with a 12-bit DAC (MCP4921) to set the regulator pressure. We also included an emergency stop button and a pressure relief valve as safety mechanisms.

To measure the bending angle of the actuator, we change the input pressure in small increments (about 10 kPa) up to 260 kPa or until the actuator reaches the negative of the initial bending angle. Bending angle data is recorded with both increasing and decreasing pressure increments to capture any hysteresis. We use OpenCV [24] to calculate the actuator's bending angle from photographs taken at each pressure increment. To isolate the high-contrast line drawn along the inextensible layer, we perform a color conversion and identify points along the contour line, as shown in Fig. 4B. Using 100 random samples along the curve, we calculate the average curvature κ of the fiberglass layer of length l_0 and convert it to a bending angle using $\psi = \kappa l_0$.

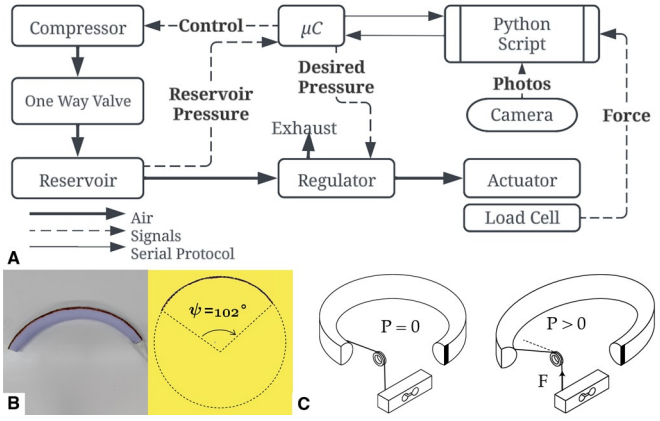

Fig. 4. A. Block diagram of the experimental setup. B. Sample of a calculated bending angle: original photo and extracted contour line with calculated bending angle. C. Blocked force experimental setup. A string connects the free end of the actuator to the load cell over a pulley. The black mark on the right indicates the fixed end of the actuator.

We test the full range of pressures using increasing and decreasing increments six times each for three actuators of each material.

To characterize the force generation of the actuators, we measure the force in a single axis when the actuator is blocked from uncurling. We fix one side of the actuator and tie an inextensible string to the free end. To restrict axial deformation, we run the string over a pulley and attach it to one side of a 2 kg load cell (uxcell) as shown in Fig 4C. Since the string only restricts motion through its inextensibility, the free end of the actuator can rotate with respect to the fixed end, a necessity to constrain the actuators. By allowing this rotation and by using a pulley, we can resolve a force that occurs along two axes into a single, measurable tension force F in the string, labeled in Fig. 3C.

III. RESULTS

A. Bending Angle

We characterized the bending angle of the actuators as a function of pressure and material properties. With increasing pressure, the bending angle evolved from the initially positive ψ_0, past $\psi = 0$ when the actuator was straight, to negative bending angles as the actuator curled back on itself, as shown in Fig. 5 for DS20 and SS40 actuators. The experimental and modeled relationship between input pressure and bending angle for three actuators of each material is shown in Fig. 6.

At angles near ψ_0, we observed little change with applied pressure and the axial and circumferential strains remained low. As the actuator approached and passed the straight $\psi = 0$ point, rapid changes in bending angle occurred with small changes in pressure. We note that the radius of curvature is unbounded as the bending angle approaches 0, making this straight position unstable, especially for softer materials.

As shown in Fig. 6, both the DS20 and DS30 actuators exhibit a total range of motion of more than double the initial bending angle within the given pressure range: 436° in 112 kPa and 424° in 175 kPa, respectively. The SS40 and

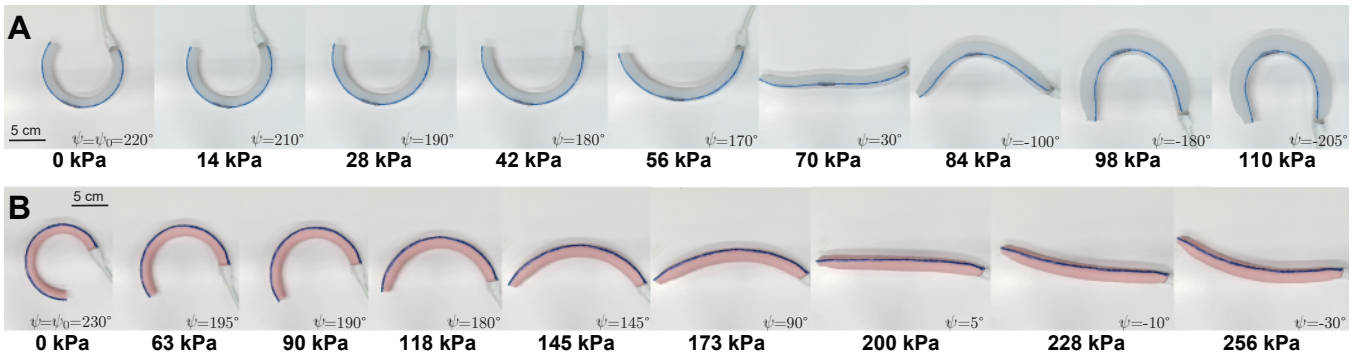

Fig. 5. Evolution of the circular actuator's unconstrained bending behavior under increasing pressure. Actuators are in a horizontal plane. A: DS20 with pressures between 0–110 kPa, negative bending angles begin at 70 kPa. B: SS40 with pressures between 0–256 kPa, with curling behavior beginning at 200 kPa.

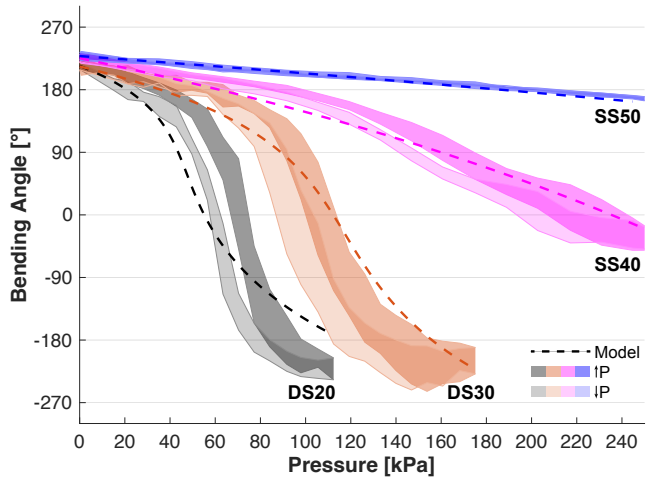

Fig. 6. Experimental results of bending angle versus input pressure for actuators of each material. The dashed lines represent the analytical model predictions. The shaded region represents one standard deviation of experimental results; darker and lighter shading represents increasing and decreasing pressure, respectively.

SS50 actuators achieve 265° and 64° respectively in 255 kPa, the upper limit for the experimental setup.

In the photos in Fig. 5, we saw that the soft DS20 actuator has a larger change in bending angle for a similar pressure increment where ψ is near 0° than the stiffer SS40 actuator does at the same angle. On average, the DS20, DS30, and SS40 actuators reached $\psi = 0$ at about 65, 105, and 215 kPa, respectively. Additionally, the model predicted the SS50 would reach $\psi = 0$ at 674 kPa, and that the SS40 would reach $\psi = -\psi_0$ at 378 kPa, but we could not verify these pressures with our experimental setup.

As the bending angle decreased past $\psi = 0$, the actuator's inner radius, a, increased rapidly and the circumferential expansion was no longer uniform along the length of the actuator, expanding more in the center than at the ends. This deformation created a non-constant curvature, as seen in DS20 near the maximum pressure of 110 kPa in Fig. 5A. Therefore, the larger uncertainty in Fig. 6 at pressures above 80 kPa for DS20 and 140 kPa for DS30 can be attributed to the constant curvature assumption in the calculated bending angle.

Actuators made of softer materials demonstrated less repeatable bending behavior, even with a single actuator, and more hysteresis than the stiffer materials, as shown in Fig. 6. The actuators required less pressure for a specified bending angle when decreasing pressure compared to increasing pressure due to the non-linear material properties of silicone. We associate the larger uncertainty in the softer materials with larger strains and the more significant non-axial deformation.

The analytical model captured the bending behavior of the actuators, particularly the change in concavity between lower and higher strains. The RMS error between the predicted bending angle and the average experimental data, including both increasing and decreasing pressure increments, is 74° for DS20, 68° for DS30, 32° for SS40, and 4.5° for SS50. The larger error in the softer materials was a function of both the large hysteresis in the experimental results and the uncertainty in the material models. Assuming incompressibility yields an underestimation of the required pressure for positive bending angles and an overestimation for negative bending angles. We verified the cross-sectional behavior by measuring the overall height of the actuator from experimental photographs, however the model does not include changes in the base layer b, which does visibly bulge at higher pressures. Future optimization of the model will require thorough material characterization to better account for stiffness non-linearities. The incorporation of additional wall thickness and volumetric measurements will also allow a more accurate model of the cross-sectional changes.

B. Blocked Force

The circular actuators have a non-linear relationship between pressure and blocked force, particularly at higher pressures and strains, as shown in Fig. 7A. On average, the DS20 actuators achieved 2.7 N of blocked force at 105 kPa. DS30 achieved 2.1 N at 112 kPa. At 210 kPa, SS40 and SS50 achieved 5.1 and 1.6 N, respectively. At lower pressures, under 40 kPa, all materials generated similar forces, as differences in material properties have less influence at smaller strains. At higher pressures, however, generating a

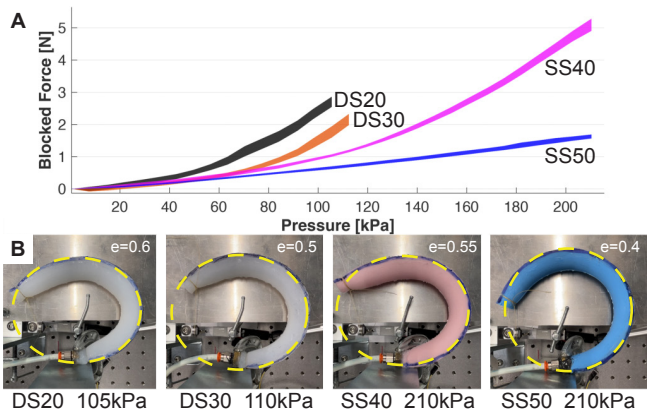

Fig. 7. A. Blocked force for actuators of each material at different input pressures. Shaded region represents one standard deviation. B. Photos of the circular actuators at the maximum pressure during blocked force testing. The yellow dashed line represents the ellipses used to measure eccentricity.

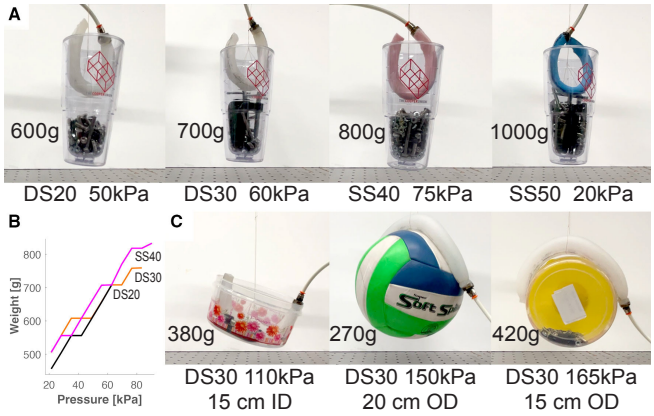

Fig. 8. A. Photographs of actuators inside an object of 9 cm inner diameter. B. Maximum weight held by different material actuators inside an object of 9 cm inner diameter. C. Photographs of a DS30 actuator grasping objects from both the inside and the outside, supported by a string in the middle.

given force required more pressure for stiffer materials. At 100 kPa, DS20 generated 1 N more force than DS30. At 210 kPa, the SS40 generated about 3 N more force than the SS50. We attribute these differences to the different bending angles the actuators would have exhibited at each pressure if unconstrained, with larger unconstrained angles corresponding to higher blocked force. The pressures of the highest force readings for DS20 and DS30 were past the $\psi = 0$ point for both materials, where an unconstrained actuator would have generated negative bending angles.

We hypothesize that two main effects contribute to the non-linearity of the blocked force results: circumferential deformation and the eccentricity formed by the actuator. Though the axial strain was restricted by fixing both ends of the actuator, internal pressure still induced circumferential expansion and thus a proportional axial stress, which increased the force F on the load cell as shown in Fig. 3C. In reaction to the axial stress, the actuator formed an elliptical shape with non-constant curvature.

To initially characterize the complex relationship between deformed shape and blocked force, we measured the eccentricity of the ellipse formed by the inextensible layer at the maximum input pressure (Fig. 7B). The eccentricity of each actuator increased with increasing input pressure. Stiffer actuators had smaller eccentricities, even at higher pressures, than softer actuators, due to less circumferential and radial deformation and therefore less axial deformation. At the maximum pressure of 105 kPa, the DS20 actuator displayed an eccentricity of 0.6, while at the higher pressure of 120 kPa, the DS30 actuator displayed a lower eccentricity of 0.5. At an even higher pressure, of 210 kPa, the SS40 and SS50 actuators displayed 0.55 and 0.4, respectively.

C. Object Grasping

When used as a simple gripper, a single circular actuator grasped objects from both the inside and outside with positive input pressure. To ensure contact with round objects and an even applied force from both sides of the actuator, we supported the actuator from the middle of its length. Fig. 8A shows circular actuators holding an object with an inner diameter of 9 cm (smaller than the initial bending radius of the actuator) with increasing weight. This object blocked the actuators at an eccentricity of approximately 0.7. When placed inside the object, all three actuators (DS20, DS30, and SS40) held 700 g within a pressure range of 0-60 kPa as shown in Fig. 8B. After 60 kPa, the DS20 actuator exerted enough force that it buckled and was thus unable to maintain contact with the object. The DS30 and SS40 actuators remained inside the object up to 80 kPa, where they held 750 g and 800 g, respectively. Increasing material stiffness provided the ability to hold about 50 g more weight for a given input pressure. The stiffest SS50 actuator held the object weighing 1000 g with an input pressure of only 20 kPa. This difference in performance was due in part to the elastic force developed in the material by compressing the actuator to fit inside the object. Additionally, the compression of the stiffer actuators allowed some weight to be supported with no input pressure and only elastic forces. This could be used in an automated system by initializing the actuator in the pressurized $\psi = 0°$ state and releasing the pressure to grasp, though this behavior requires further investigation.

Additionally, we demonstrated the basic capabilities of the actuator for objects of varying sizes and weights. Holding larger objects required an initial input pressure to generate a curvature corresponding to the object's inner or outer diameter and additional pressure to generate a gripping force. As shown in Fig. 8C, a DS30 circular actuator at 110 kPa grasped a 15 cm diameter object weighing 380 g from the inside and a 420 g object of the diameter from the outside at 165 kPa. A single DS30 actuator also held a 270 g volleyball of 20 cm outer diameter at 150 kPa. These weights are not the maximum weight the actuator could hold but a demonstration of the grasping capabilities for these larger objects. This initial characterization found that as the diameter of an object decreases or the weight increases, more pressure is required to hold the object from either the inside or outside.

IV. CONCLUSIONS AND FUTURE WORK

This paper has presented the design, fabrication, modeling, and experimental results characterizing the behavior of a circular soft pneumatic actuator capable of bi-directional bending. Our circular actuators, made of a uniform soft material, can uncurl and curl back on themselves with increasing pressure in a single chamber. In bending angle experiments, we found that the softer DS20 and DS30 actuators were able to reach at least the negative of their initial bending angle with an input pressure of under 150 kPa. Our analytical model, which captures both axial and circumferential deformation, accurately predicted the relationship between bending angle and input pressure for actuators of varying stiffness. In blocked force experiments, we found that the actuators can generate 1.6–5.1 N of force, depending on the material. We also demonstrated the circular actuator's ability to grasp objects of various diameters and weights up to 1 kg from both the inside and outside of the object when supported from the midpoint of its length.

Future work will expand the analytical model to better characterize the cross-sectional behavior as well as to explore the relationships between input pressure, blocked force, and the eccentricity formed by the actuator when constraining axial deformation. Additionally, we will develop a finite element model to better account for the non-linear elasticity and the complex deformations, particularly at high input pressures and due to contact. The ability to fully characterize the circular actuator's bending and blocked force behavior will allow for robust control at all pressures. We plan to integrate the actuator as a robotic end effector and to implement a closed-loop feedback control scheme, employing its entire range of motion for force-based grasping applications.

The use of a single chamber and a uniform material with one control signal to create a vast range of bending angles allows for simpler fabrication and more straightforward control. Adding the circular shape during fabrication allows new possibilities to increase adaptability, achievable bending behaviors, and performance capabilities in soft robotics.

ACKNOWLEDGMENTS

The authors thank Elise Danko, Ruslana Bukalo, Erika Gregory, Claire Park, Sophia Xu, and Randel Placino for fabricating dozens of actuators. Joya Debi for writing experimentation software. Doug Thornhill, James Edward Malin, Jacob Koziej, C.R. Van West, Ridwan Hussain, Jon Lu, and Brett Circe for unyielding support and advice.

REFERENCES

[1] C. Laschi, B. Mazzolai, and M. Cianchetti, "Soft robotics: Technologies and systems pushing the boundaries of robot abilities," *Science Robotics*, vol. 1, p. eaah3690, Dec. 2016.

[2] Y. Hotoda and K. Ito, "Octopus-Like Soft Robot Hand for Handling Vegetables and Fruits," in *2023 International Conference on Advanced Mechatronic Systems (ICAMechS)*, (Melbourne, Australia), pp. 13–18, IEEE, Sept. 2023.

[3] K. C. Galloway, P. Polygerinos, C. J. Walsh, and R. J. Wood, "Mechanically programmable bend radius for fiber-reinforced soft actuators," in *2013 16th International Conference on Advanced Robotics (ICAR)*, (Montevideo, Uruguay), pp. 1–6, IEEE, Nov. 2013.

[4] M. McCandless, A. Perry, N. DiFilippo, A. Carroll, E. Billatos, and S. Russo, "A Soft Robot for Peripheral Lung Cancer Diagnosis and Therapy," *Soft Robotics*, vol. 9, pp. 754–766, Aug. 2022.

[5] D. R. Ellis, M. P. Venter, and G. Venter, "Generative Design Procedure for Embedding Specified Planar Behavior in Modular Soft Pneumatic Actuators," *Soft Robotics*, vol. 9, pp. 552–561, June 2022.

[6] R. A. Bilodeau, M. C. Yuen, J. C. Case, T. L. Buckner, and R. Kramer-Bottiglio, "Design for Control of a Soft Bidirectional Bending Actuator," in *2018 IEEE/RSJ International Conference on Intelligent Robots and Systems (IROS)*, (Madrid), pp. 1–8, IEEE, Oct. 2018.

[7] A. Pagoli, F. Chapelle, J. A. Corrales, Y. Mezouar, and Y. Lapusta, "A Soft Robotic Gripper With an Active Palm and Reconfigurable Fingers for Fully Dexterous In-Hand Manipulation," *IEEE Robotics and Automation Letters*, vol. 6, pp. 7706–7713, Oct. 2021.

[8] H. Feng, Y. Sun, P. A. Todd, and H. P. Lee, "Body Wave Generation for Anguilliform Locomotion Using a Fiber-Reinforced Soft Fluidic Elastomer Actuator Array Toward the Development of the Eel-Inspired Underwater Soft Robot," *Soft Robotics*, vol. 7, pp. 233–250, Apr. 2020.

[9] D. Q. Nguyen and V. A. Ho, "Anguilliform Swimming Performance of an Eel-Inspired Soft Robot," *Soft Robotics*, vol. 9, pp. 425–439, June 2022.

[10] D. D. K. Arachchige, D. M. Perera, S. Mallikarachchi, I. Kanj, Y. Chen, and I. S. Godage, "Wheelless Soft Robotic Snake Locomotion: Study on Sidewinding and Helical Rolling Gaits," in *2023 IEEE International Conference on Soft Robotics (RoboSoft)*, (Singapore, Singapore), pp. 1–6, IEEE, Apr. 2023.

[11] Y. Fei, J. Wang, and W. Pang, "A Novel Fabric-Based Versatile and Stiffness-Tunable Soft Gripper Integrating Soft Pneumatic Fingers and Wrist," *Soft Robotics*, vol. 6, pp. 1–20, Feb. 2019.

[12] M. Ariyanto, M. Munadi, J. D. Setiawan, D. Mulyanto, and T. Nugroho, "Three-Fingered Soft Robotic Gripper Based on Pneumatic Network Actuator," in *2019 6th International Conference on Information Technology, Computer and Electrical Engineering (ICITACEE)*, (Semarang, Indonesia), pp. 1–5, IEEE, Sept. 2019.

[13] M. Fatahillah, N. Oh, and H. Rodrigue, "A Novel Soft Bending Actuator Using Combined Positive and Negative Pressures," *Frontiers in Bioengineering and Biotechnology*, vol. 8, p. 472, May 2020.

[14] B. Gorissen, D. Reynaerts, S. Konishi, K. Yoshida, J. Kim, and M. De Volder, "Elastic Inflatable Actuators for Soft Robotic Applications," *Advanced Materials*, vol. 29, p. 1604977, Nov. 2017.

[15] E. Perez-Guagnelli and D. D. Damian, "Deflected Versus Preshaped Soft Pneumatic Actuators: A Design and Performance Analysis Toward Reliable Soft Robots," *Soft Robotics*, vol. 9, pp. 713–722, Aug. 2022.

[16] A. Al-Ibadi, S. Nefti-Meziani, and S. Davis, "A circular pneumatic muscle actuator (CPMA) inspired by human skeletal muscles," in *2018 IEEE International Conference on Soft Robotics (RoboSoft)*, (Livorno), pp. 7–12, IEEE, Apr. 2018.

[17] L. Hu, D. Gau, J. Nixon, M. Klein, Y. Fan, G. Menary, and E. T. Roche, "Precurved, Fiber-Reinforced Actuators Enable Pneumatically Efficient Replication of Complex Biological Motions," *Soft Robotics*, vol. 9, pp. 293–308, Apr. 2022.

[18] P. Polygerinos, Z. Wang, J. T. B. Overvelde, K. C. Galloway, R. J. Wood, K. Bertoldi, and C. J. Walsh, "Modeling of Soft Fiber-Reinforced Bending Actuators," *IEEE Transactions on Robotics*, vol. 31, pp. 778–789, June 2015.

[19] F. Connolly, C. J. Walsh, and K. Bertoldi, "Automatic design of fiber-reinforced soft actuators for trajectory matching," *Proceedings of the National Academy of Sciences*, vol. 114, pp. 51–56, Jan. 2017.

[20] L. Marechal, P. Balland, L. Lindenroth, F. Petrou, C. Kontovounisios, and F. Bello, "Toward a Common Framework and Database of Materials for Soft Robotics," *Soft Robotics*, vol. 8, pp. 284–297, June 2021.

[21] A. Pagoli, F. Chapelle, J.-A. Corrales-Ramon, Y. Mezouar, and Y. Lapusta, "Review of soft fluidic actuators: classification and materials modeling analysis," *Smart Materials and Structures*, vol. 31, p. 013001, Jan. 2022.

[22] M. S. Xavier, A. J. Fleming, and Y. K. Yong, "Finite Element Modeling of Soft Fluidic Actuators: Overview and Recent Developments," *Advanced Intelligent Systems*, vol. 3, p. 2000187, Feb. 2021.

[23] L. Paternò, G. Tortora, and A. Menciassi, "Hybrid Soft–Rigid Actuators for Minimally Invasive Surgery," *Soft Robotics*, vol. 5, pp. 783–799, Dec. 2018.

[24] G. Bradski, "The OpenCV Library," *Dr. Dobb's Journal of Software Tools*, 2000.